

Chirp-Scaling Algorithm for Bistatic SAR Data in the Constant-Offset Configuration

Robert Wang, *Member, IEEE*, Otmar Loffeld, *Senior Member, IEEE*, Holger Nies, Stefan Knedlik, *Member, IEEE*, and Joachim H. G. Ender, *Senior Member, IEEE*

Abstract—This paper discusses the processing method for bistatic SAR data in the constant-offset configuration. The constant-offset configuration is also known as the azimuth stationary or invariant configuration where transmitter and receiver follow each other, moving on identical velocity vector. In this paper, the proposed processing method for bistatic SAR data is based on Loffeld's bistatic formula that consists of two terms, i.e., the quasi-monostatic (QM) term and bistatic-deformation (BD) term. Our basic idea is to linearize the aforementioned two terms and then incorporate the BD term into the QM term to obtain an analogous monostatic spectrum. Based on the new spectrum, any efficient 2-D frequency or range-Doppler domain processor can easily be employed to process the bistatic data, where the Doppler phase parameters of the processor need to be adjusted. In this paper, we concentrate on the application of chirp-scaling-algorithm (CSA) processor. In addition, a bistatic-motion error model is developed where the position deviations of the two platforms are simplified as the bistatic slant-range displacement in the zero Doppler plane. Using this model, the monostatic motion-compensation technique is applied and integrated into CSA to compensate the trajectory deviations of transmitter and receiver. Finally, real and simulated data are used to validate the proposed processing method.

Index Terms—Bistatic SAR, Fourier transform (FT), motion compensation (MOCO), range cell migration (RCM).

NOMENCLATURE

s	Azimuth time variable.
c	Speed of light.
s_{0R}, s_{0T}	Zero Doppler times of receiver and transmitter.
R_{0R}, R_{0T}	Closest ranges from receiver and transmitter to the point target $P(s_{0R}, R_{0R})$.
(s_{0R}, R_{0R})	Receiver-referenced coordinates, defined as the coordinates of image space.
$\sigma(s_{0R}, R_{0R})$	Backscattering coefficient of the point target located at (s_{0R}, R_{0R}) .
$\bar{R}_{0R}, \bar{R}_{0T}$	Closest ranges from receiver and transmitter to the point target $P(s_{0R}, R_{0R})$ in the presence of trajectory deviations.

R_m	Closest range from the scene center to the ideal trajectory of receiver.
r	Zero-offset receiver-to-target range variable defined by $r = R_{0R} - R_m$.
$R_R(s), R_T(s)$	Instantaneous slant ranges from receiver and transmitter to the point target $P(s_{0R}, R_{0R})$.
$\bar{R}_R(s), \bar{R}_T(s)$	Instantaneous slant ranges from receiver and transmitter to the point target $P(s_{0R}, R_{0R})$ with trajectory deviations.
v_R, v_T	Platform velocities of receiver and transmitter; in the constant-offset configuration, we have $v_R = v_T = v$.
H_{0R}, H_{0T}	Nominal platform heights of receiver and transmitter.
d_1, d_2	Constant offsets orthogonal to and along the flight track direction.
λ, f_0	Carrier wavelength and carrier frequency of the transmitted signal.
f, f_a	Frequency variables corresponding to range time and azimuth time.
a_0	Zero Doppler time difference between transmitter and receiver, $a_0 = s_{0T} - s_{0R}$.
θ_{RS}, θ_{TS}	Azimuth beam width of receiver and transmitter, respectively.

I. INTRODUCTION

FOR THE bistatic SAR processing, the time-domain methods can focus the bistatic SAR data well. However, focusing in the time domain is paid for by a huge computational cost. The efficiency of processing can be highly improved by performing bistatic SAR focusing in the frequency domain. Therefore, frequency-domain methods are preferred. Based on Loffeld's bistatic formula (LBF) [1], the inversed scaled Fourier transform (ISFT) is used to process the bistatic SAR data in the constant-offset or general configurations [2], [3]. In [1], bistatic-deformation (BD) term is considered as a residual phase and removed blockwise by using phase multiplication. In every segmented block, the variant slant-range variables are replaced with their mean values. Blockwise operation, however, implies an increase of computational cost. In [4], a preprocessing technique known as Dip Move Out is employed to transform the bistatic constant-offset configuration to the monostatic one. The wavenumber-domain algorithm (WDA) to process the bistatic SAR data is described in [5] and [6]. In [7], the range-Doppler algorithm (RDA) and extended chirp-scaling algorithm (CSA) are also proposed to process the constant-offset bistatic

Manuscript received December 20, 2007; revised July 23, 2008 and August 20, 2008. First published December 12, 2008; current version published February 19, 2009. This work was supported by the Germany Science Foundation under Grant Lo 455/7-1 BiFocus.

R. Wang, O. Loffeld, H. Nies, and S. Knedlik are with the Center for Sensorsystems (ZESS), University of Siegen, 57076 Siegen, Germany (e-mail: wang@zess.uni-siegen.de).

J. H. G. Ender is with the Research Institute for High Frequency Physics and Radar Techniques (FHR), Forschungsgesellschaft für Angewandte Naturwissenschaften (FGAN), 53343 Wachtberg, Germany.

Color versions of one or more of the figures in this paper are available online at <http://ieeexplore.ieee.org>.

Digital Object Identifier 10.1109/TGRS.2008.2006275

SAR data where a second-order approximation is applied to the slant-range histories. A numeric transfer function for bistatic SAR is developed in [8]. Using the numeric transfer function, standard SAR processor can be used to process the bistatic SAR data in the constant-offset configurations. In addition, a modified RDA is proposed to the space-surface bistatic SAR data in the general configuration [9]. In particular, based on an analytical bistatic point-target reference spectrum (BPTRS) [10], a nonlinear CSA (NLCS) has been used to process the bistatic SAR data in the general configuration [11]. For NLCS, the chirp-scaling operation is performed not to correct range cell migration (RCM) but equalize the azimuth chirp rate.

The results developed in this paper are mainly based on LBF that is an approximate BPTRS [1]. In the Doppler domain, the multiplication of BD and quasi-monostatic (QM) terms implies, that the inverse FTs of their phase terms are convolved in the azimuth time domain. It is the convolution that makes the bistatic slant-range history to lose the hyperbolic form and show a flat-top shape [1], [4]. The flat-top hyperbola is also the reason that monostatic SAR processing methods cannot be applied directly.

In the following work, we will derive a method to incorporate the BD term into the QM term, overcoming the limitation to first compensate the BD by blockprocessing. After incorporating, we have a better accuracy and efficiency as compared with our previous work [2], which means larger blocks or no blocks at all. We do this by individually linearizing BD and QM in terms of slant range, superimposing both contributions and separating the outcoming results into range-variant and range-invariant parts. For linearization, we express the transmitter-to-target range as a function of the receiver-to-target range. The purpose of doing so is to change the bistatic geometry to a receiver-referenced geometry and overcome the limitation of the flat-top hyperbola.

The CSA is an excellent method, since it efficiently corrects the RCM without interpolation [12], [13]. Therefore, in this paper, we prefer to discuss the application of CSA in the bistatic SAR data processing. To facilitate the application of CSA, the range-variant and range-invariant terms are expanded as a series in terms of the range frequency. From the range-variant term, we keep the first-order range-frequency term, while for the range-invariant term, we truncate the series at the second-order frequency term.

As far as the airborne bistatic SAR systems are concerned, trajectory deviation of sensor can strongly degrade the final image quality in the form of geometrical inaccuracies and radiometric-resolution losses [14]. To account for the deviations, flight parameters are measured onboard using the global positioning system (GPS), and inertial navigation system (INS) [3], [14]. Using the measured position information, a motion-compensation (MOCO) method can be applied to improve the quality of focused image. For the bistatic airborne SAR system, the trajectory deviations are more complex with respect to the monostatic SAR, since both transmitter and receiver contribute to the deviations [3]. In [3], the effect of deviations on the shift of the Doppler spectrum is concerned. In this paper, we model the trajectory derivations of transmitter and receiver as the bistatic slant-range displacement in the zero Doppler

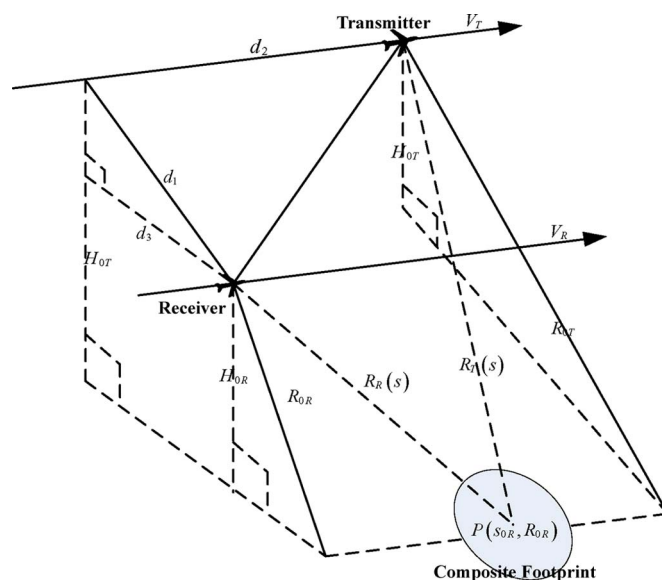


Fig. 1. Nominal geometry of the bistatic SAR in the constant-offset configuration.

plane (ZDP) and, then, divide the displacement into the range-invariant and range-variant terms. Applying this model of bistatic trajectory deviations, the conventional monostatic two-step MOCO technique can be applied to eliminate the displacements [14], [15].

This paper is organized as follows. In Section II, the bistatic signal model and linearization of the LBF are developed; in addition, the spectrum of the whole bistatic scene is derived. Section III begins with the spectrum and presents the CSA for the bistatic SAR data. In Section IV, we discuss the model of the bistatic trajectory deviations and develop MOCO method. Then, processing of simulated and real data is used to validate the presented model and method in Section V. Finally, some conclusions are reported in Section VI.

II. BISTATIC SAR SIGNAL MODEL

In this paper, we consider the bistatic geometry in the constant-offset configuration, shown in Fig. 1. The mathematical symbols and their definitions used in this paper are given in the Nomenclature.

We start from the point-target reference spectrum of the bistatic SAR signal derived in [2]. It is rewritten as

$$\begin{aligned}
G(f_a, f, R_{0R}) &= \sigma(s_{0R}, R_{0R}) S_1(f) w(s_p - s_{cb}) \\
&\times \exp[-j\Psi_{\text{QM}}(f_a, f, R_{0R})] \\
&\times \exp\left[-j\frac{\Psi_{\text{BD}}(f_a, f, R_{0R})}{2}\right] \quad (1)
\end{aligned}$$

where we ignore the inessential amplitude and phase terms. $S_1(f)$ is the baseband spectrum of the transmitted signal and is assumed to have a positive chirp rate; $w(s_p - s_{cb})$ is the composite azimuth antenna pattern centered on azimuth time s_{cb} ; s_p is the common point of stationary phase; in the azimuth frequency domain, it will be simplified as a rectangular window

around the bistatic Doppler centroid f_{Dc} with the bistatic Doppler bandwidth B_a . Ψ_{QM} and Ψ_{BD} represent the QM and BD phase terms, respectively. The complete expression of QM and BD are given as

$$\Psi_{QM}(f_a, f, R_{0R}) = \pi f_a(s_{0T} + s_{0R}) + \frac{2\pi}{c} R_{0R} F_R + \frac{2\pi}{c} R_{0T} F_T \quad (2)$$

$$\Psi_{BD}(f_a, f, R_{0R}) = \frac{2\pi v_R^2 v_T^2 F_R^3 F_T^3}{c(f + f_0)^2 (R_{0R} v_T^2 F_T^3 + R_{0T} v_R^2 F_R^3)} \times \left[(s_{0T} - s_{0R}) - \frac{c f_a}{2v_R^2 v_T^2 F_R F_T} \times (R_{0T} v_R^2 F_R - R_{0R} v_T^2 F_T) \right]^2 \quad (3)$$

where

$$F_{R,T} = \sqrt{(f + f_0)^2 - (c f_a / 2v_{R,T})^2}. \quad (4)$$

The subscripts “ R ” and “ T ” denote receiver’s and transmitter’s value, respectively. The expressions given in (2) and (3) are the results, obtained for the general configuration. In this paper, we mainly consider the constant-offset case where transmitter and receiver move with the identical velocity v . Hence, (4) can be rewritten as $F_x = \sqrt{(f + f_0)^2 - (c f_a / 2v)^2}$. Substituting F_x into (2) and (3) yields

$$\Psi_{QM}(f_a, f, R_{0R}) = \pi f_a(s_{0T} + s_{0R}) + \frac{2\pi}{c} (R_{0R} + R_{0T}) F_x \quad (5)$$

$$\Psi_{BD}(f_a, f, R_{0R}) = \frac{2\pi v^2 F_x^3}{c(f + f_0)^2 (R_{0T} + R_{0R})} \times \left[(s_{0T} - s_{0R}) - \frac{c f_a}{2v^2 F_x} (R_{0T} - R_{0R}) \right]^2. \quad (6)$$

Equation (5) is similar to the spectrum of monostatic SAR signal and corresponds to the normal hyperbolic range history. Equation (6) is caused by the spatially separated platforms and, hence, describes the intrinsic feature of a bistatic SAR signal.

In [2], the BD term is removed using phase multiplications in segmented range blocks to handle the principally range-variant feature of (6). In this paper, our basic idea is to incorporate the BD term into the QM term, using linearized expressions; we will develop an expression of BPTRS that is linearly dependent on r . The new expression can make any efficient monostatic processing algorithm applicable.

From (5) and (6), it can be seen that the BD term nonlinearly depends on R_{0T} and R_{0R} . In order to address this problem, a geometric transformation method is used. According to the previous definition, R_{0R} can be expressed as the sum of a linearly variant term r and invariant term R_m . We can use the geometric image transformation [16] to map R_{0T} onto R_{0R} and further express R_{0R} as a function of r and R_m .

Supposing the horizontal geometry of earth surface, the one-to-one relationship between R_{0R} and R_{0T} can be formulated as

$$R_{0T} = \sqrt{H_{0T}^2 + \left[d_3 + \sqrt{(r + R_m)^2 - H_{0R}^2} \right]^2} \quad (7)$$

where d_3 is projection of d_1 in the broadside direction. Using (7) and the definition $r = R_{0R} - R_m$, the slant-range terms involved in (5) and (6) can be expanded as the first-order Taylor series in terms of r/R_m

$$R_{0T} + R_{0R} = c_0 R_m + c_1 r \quad (8)$$

$$1/(R_{0R} + R_{0T}) = (c_2 + c_3 r)/R_m$$

$$(R_{0T} - R_{0R})/(R_{0T} + R_{0R}) = c_4 + c_5 r$$

$$(R_{0T} - R_{0R})^2/(R_{0T} + R_{0R}) = c_6 R_m + c_7 r \quad (9)$$

where $c_0 R_m$, c_2/R_m , c_4 , and $c_6 R_m$ denote the invariant components of the slant-range terms and c_1 , c_3 , c_5 , and c_7 represent the coefficients of the variant components of the slant-range terms. Then, a direct substitution of (8) and (9) and the definition $a_0 = s_{0T} - s_{0R}$ into (5) and (6) yield the new expressions of the QM and BD terms as

$$\Psi_{QM}(f_a, f, R_{0R}) = \left[\pi f_a(a_0 + 2s_{0R}) + \frac{2\pi c_0 R_m}{c} F_x \right] + \frac{2\pi c_1 F_x}{c} r \quad (10)$$

$$\Psi_{BD}(f_a, f, R_{0R}) = \left[\frac{2\pi c_2 v^2 a_0^2 F_x^3}{c(f + f_0)^2 R_m} - \frac{2\pi a_0 c_4 F_x^2 f_a}{(f + f_0)^2} + \frac{c c_6 \pi F_x f_a^2 R_m}{2v^2 (f + f_0)^2} \right] + \left[\frac{2\pi c_3 v^2 a_0^2 F_x^3}{c(f + f_0)^2 R_m} - \frac{2\pi a_0 c_5 F_x^2 f_a}{(f + f_0)^2} + \frac{c c_7 \pi F_x f_a^2}{2v^2 (f + f_0)^2} \right] r. \quad (11)$$

Then, combining (10) and (11), decomposing them into a range-invariant and range-variant terms yields

$$\Psi_B(f_a, f, R_{0R}) = \Psi_{QM}(f_a, f, R_{0R}) + \frac{\Psi_B(f_a, f, R_{0R})}{2} = \Psi_{IV}(f_a, f) + \Psi_V(f_a, f, r) \quad (12)$$

where the range-invariant and range-variant terms are denoted by the subscript IV and V

$$\Psi_{IV}(f_a, f) = \left[\pi a_0 f_a + \frac{2\pi c_0 R_m}{c} F_x \right] + \frac{1}{2} \left[\frac{2\pi c_2 v^2 a_0^2 F_x^3}{c(f + f_0)^2 R_m} - \frac{2\pi a_0 c_4 F_x^2 f_a}{(f + f_0)^2} + \frac{\pi c c_6 F_x f_a^2 R_m}{2v^2 (f + f_0)^2} \right] \quad (13)$$

$$\Psi_V(f_a, f, r) = 2\pi s_{0R} f_a + \frac{2\pi c_1 F_x}{c} r + \frac{1}{2} \left[\frac{2\pi c_3 v^2 a_0^2 F_x^3}{c(f + f_0)^2 R_m} - \frac{2\pi a_0 c_5 F_x^2 f_a}{(f + f_0)^2} + \frac{\pi c c_7 F_x f_a^2}{2v^2 (f + f_0)^2} \right] r. \quad (14)$$

Equation (13) describes the space-invariant features of the bistatic SAR signal and (14) shows the space-variant features. Using (13) and (14), any efficient monostatic algorithm can be applied to focus the bistatic SAR data. However, in this paper, we consider CSA, requiring some further approximation. Equations (13) and (14) are expanded in Taylor series in terms of f/f_0 , giving the following results:

$$\Psi_{IV}(f_a, f) \approx \Phi_{aIV}(f_a) + 2\pi t_{mc}f + \frac{\pi f^2}{K_{src}} + \dots \quad (15)$$

$$\Psi_V(f_a, f, r) \approx 2\pi s_{0R}f_a + 2\pi\Phi_{aV}(f_a)r + 2\pi \left(\frac{2r}{c} \right) (Cs + 1)f + \dots \quad (16)$$

where

$$\begin{aligned} \Phi_{aIV}(f_a) = & \pi a_0 f_a \\ & + \left[\frac{2\pi c_0 R_m}{\lambda} D + \frac{\pi c_2 a_0^2 v^2 D^3}{\lambda R_m} \right. \\ & \left. - \pi a_0 c_4 D^2 f_a + \frac{\pi \lambda c_6 R_m D f_a^2}{4v^2} \right] \end{aligned} \quad (17)$$

$$\begin{aligned} t_{mc}(f_a) = & \left(\frac{2R_m}{c} \right) \\ & \times \left[\frac{c_0}{2D} + \frac{c_2 v^2 a_0^2 (6D - 5D^3)}{4cR_m^2} \right. \\ & \left. - \frac{a_0 c_4 \lambda f_a (1 - D^2)}{2R_m} + \frac{c_6 \lambda^2 (2 - 3D^2) f_a^2}{16v^2 D} \right] \end{aligned} \quad (18)$$

$$\begin{aligned} \frac{1}{K_{src}(f_a)} = & - \frac{c_0 (1 - D^2) R_m}{\lambda D^3 f_0^2} \\ & + \frac{3c_2 v^2 a_0^2 (1 - D^2) (2 - 3D^2)}{\lambda R_m D f_0^2} \\ & + \frac{3c_4 a_0 f_a (1 - D^2)}{f_0^2} \\ & - \frac{\lambda c_6 f_a^2 R_m (7D^4 - D^2 - 4)}{8v^2 f_0^2 D^3} \end{aligned} \quad (19)$$

$$\Phi_{aV}(f_a) = \left[\frac{c_1 D}{\lambda} + \frac{c_3 v^2 a_0^2 D^3}{2\lambda R_m} - \frac{a_0 c_5 D^2 f_a}{2} + \frac{\lambda c_7 D f_a^2}{8v^2} \right] \quad (20)$$

$$\begin{aligned} Cs(f_a) = & -1 \\ & + \left[\frac{c_1}{2D} + \frac{c_3 v^2 a_0^2 (6D - 5D^3)}{4R_m} \right. \\ & \left. - \frac{a_0 c_5 \lambda f_a (1 - D^2)}{2} + \frac{c_7 \lambda^2 (2 - 3D^2) f_a^2}{16v^2 D} \right] \end{aligned} \quad (21)$$

where D is defined as $\sqrt{1 - (\lambda f_a / 2v)^2}$. Some short remarks concerning (15)–(21) will be helpful to understand the idea.

- 1) Equation (15) can be expanded up to any order. Here, the higher order terms than the second order are ignored. However, for extremely high squinted geometries, the effect of the higher order terms (e.g., cubic and quartic) must be taken into account [12], [16].
- 2) Equation (16) is truncated at the first-order term, since the higher order terms have a weak dependence on the variant component of the slant range.
- 3) $\Phi_{aIV}(f_a)$ represents the range-independent azimuth-modulation term and can be removed by the phase multiplication in the 2-D frequency domain.
- 4) t_{mc} is usually referred to as the time locus of the reference range in the range-Doppler domain [13]. It answers for the range-invariant RCM and is the dominant component of the total RCM.
- 5) $K_{src}(f_a)$ is an additional range chirp rate and explained as the cross coupling between range and azimuth. If uncompensated, it can cause significant degradation in the resolution, particularly in the range [12].
- 6) $\Phi_{aV}(f_a)$ is the range-variant azimuth modulation. Because of the range dependence, it has to be removed in the range-Doppler domain.
- 7) $Cs(f_a)$ is involved in the first-order range-frequency term of (16) and named as the scaling or curvature factor [13]. Its presence leads to the fact that the position of the range impulse response after compression is not determined by r but by a linearly scaled term $(Cs + 1)r$. Therefore, the scaling factor $Cs(f_a)$ describes the Doppler-dependent RCM with respect to the reference range in the Doppler domain. The task of any RCM-correction (RCMC) methods tends to make the scaling factor equal to zero, e.g., interpolation operation is applied in RDA and WDA to correct RCMC, chirp-scaling transform is used in CSA. When the bistatic configuration is reduced to the monostatic one, the scaled factor becomes $1/D - 1$, which is well known in the monostatic SAR [12], [13]. The reason for the different $Cs(f_a)$ factor in monostatic and bistatic SARs is originally caused by the nonhyperbolic slant-range histories in the bistatic case.

In the following, we derive the spectrum of the baseband scene (BS) (also called system transfer function). In reality, the received SAR data can be detected and recorded only after some delay. For convenience, we shift the sampling starting time to the middle swath. And thus, the raw data becomes the baseband signal in the slant-range domain. The shifted time is defined as $t_m = c_0 R_m / c$. After shifting the starting time to the right by t_m , the coordinate of backscattering coefficient becomes (s_{0R}, r) . We name the shifted scene as the BS. Thus, further combining (1), (12), (15), and (16) and substituting the rectangle function $\text{rect}[(f_a - f_{Dc})/B_a]$ for $w(s_p - s_{cb})$, the BPTRS of BS can be rewritten as

$$\begin{aligned} G(f_a, f, s_{0R}, r) = & \sigma(s_{0R}, r) S_1(f) \text{rect} \left[\frac{f_a - f_{Dc}}{B_a} \right] \\ & \times \exp[-j\Psi_{IV}(f_a, f)] \\ & \times \exp[-j\Psi_V(f_a, f, r)]. \end{aligned} \quad (22)$$

As the spectrum of BS is the sum of reflected signals from all the point targets, it can be expressed as [2]

$$H(f_a, f) = S_1(f) \text{rect} \left[\frac{f_a - f_{Dc}}{B_a} \right] \exp[-j\Psi_{IV}(f_a, f)] \\ \times \iint \sigma(s_{0R}, r) \times \exp[-j\Psi_V(f_a, f, r)] ds_{0R} dr \\ = G_0(f_a, f) \sigma[f_a, \Phi_{aV} + (Cs + 1)f_r] \quad (23)$$

where f_r represents the normalized range-frequency variable and is given by $f_r = 2f/c$ and $G_0(f_a, f)$ is the 2-D space-invariant component of the spectrum and given by

$$G_0(f_a, f) = S_1(f) \text{rect} \left[\frac{f_a - f_{Dc}}{B_a} \right] \exp[-j\Psi_{IV}(f_a, f)]. \quad (24)$$

From (23), it can be seen that the spectrum of BS is a scaled and shifted version of the backscattering coefficient spectrum $\sigma[f_a, f]$ in the range direction.

III. CSA

In this section, we begin with the bistatic SAR raw data. To focus the raw data, the first step is to obtain the spectrum BS. According to the shifting theorem of FT, to shift the sampling starting time by a constant time t_m to the right, its spectrum can be multiplied by a linear phase function, an exponential with a negative exponent $\exp(-j2\pi f t_m)$. Thus, the BS can be achieved by transforming the raw data into 2-D frequency domain and then multiplying it by $\exp(-j2\pi f t_m)$. Subsequently, our task is to reconstruct $\sigma(s_{0R}, r)$ from the spectrum of BS expressed by (23).

Because $G_0(f_a, f)$ is the space-invariant term in the 2-D frequency domain, it can be removed by multiplying (23) by the complex conjugate of $G_0(f_a, f)$ denoted with $G_0^*(f_a, f)$. The shifting phase factor $\exp(-j2\pi f t_m)$ can be combined with $G_0^*(f_a, f)$. The new expression of $G_0(f_a, f)$ is given by $G_1(f_a, f) = G_0(f_a, f) \times \exp(j2\pi f t_m)$. Therefore, removing space-invariant phase and shifting the scene to the baseband can be expressed as

$$H_1(f_a, f) = H(f_a, f) \times G_1^*(f_a, f) = \sigma[f_a, \Phi_{aV} + (Cs + 1)f_r]. \quad (25)$$

To express the backscattering coefficient $\sigma(s_{0R}, r)$, the subsequent task is to correct scaling and shifting. A simple method to correct them is to use the nonlinear mapping to achieve

$$\sigma[f_a, \Phi_{aV} + (Cs + 1)f_r] \rightarrow \sigma[f_a, f_r]. \quad (26)$$

This method applying the nonlinear mapping is generally called the Stolt mapping. The detailed description of the mapping is out of the scope of this paper.

In this paper, we prefer the chirp-scaling method to correct the scaling term. The derivation of chirp scaling is performed in the frequency domain by using the frequency-domain technique [16]–[18] after the step of multiplying $G_1^*(f_a, f)$. The processing scheme using frequency-scaling technique is shown in Fig. 2.

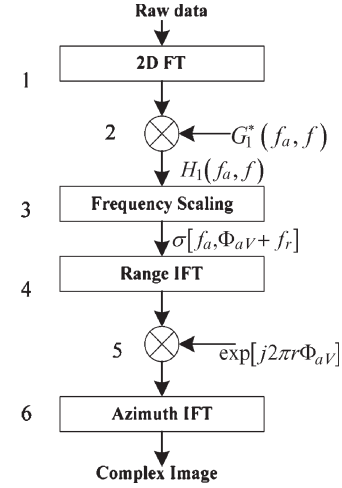


Fig. 2. Block diagram using the frequency-scaling technique to focus the bistatic image.

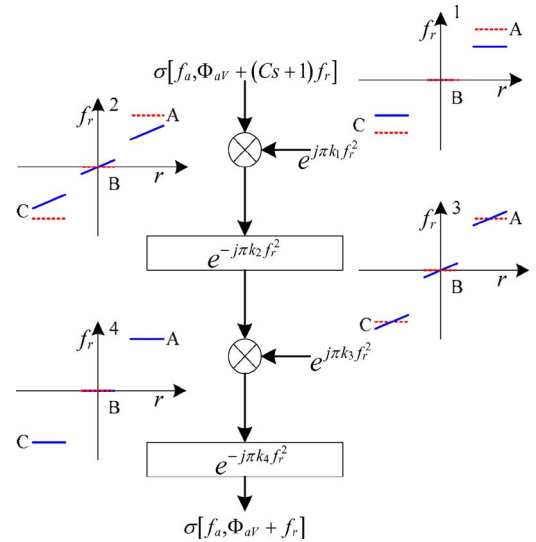


Fig. 3. Block diagram of the frequency-scaling technique. The nonessential amplitude factors are neglected.

The processing steps shown in Fig. 2 are summarized as follows.

- 1) The first step is to perform a 2-D FT to transform the data into the 2-D frequency domain.
- 2) Using phase multiplication, we remove the space-invariant phase and compress the range signal.
- 3) Frequency-scaling operation is implemented to correct RCM in the 2-D frequency domain.
- 4) An inverse FT is performed to transform the data into the range-Doppler domain.
- 5) The range-variant azimuth modulation is compensated.
- 6) Finally, an azimuth inverse FT is performed to transform the focused data into the complex image domain.

Furthermore, Fig. 3 shows an explanation of the frequency-scaling block, as shown in Fig. 2, in more detail. We consider three point targets (A, B, C). All three point targets are located at the same azimuth position, where B is located at the scene center and A and C are at far- and near-range position. For each point target, we plot its scaled frequency f_r depending on range.

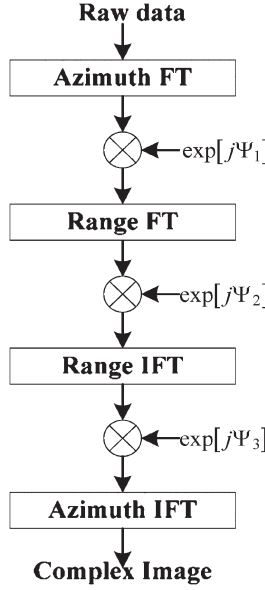


Fig. 4. Block diagram obtained from Fig. 2.

The first plot shows the results after multiplying $G_1^*(f_a, f)$ for a given azimuth frequency. At this stage, the range chirp signal and range-invariant RCM have been eliminated.

The echo signal position is determined by the first-order frequency term of (16) $(Cs + 1)rf_r$. The scaling factor Cs introduces a deviation of the signal's phase center from the real position denoted by the dotted line (red) to the migrated position denoted by the solid line (blue). The task of frequency-scaling operation is to correct the derivation.

Plot 2 shows the outcome of the first phase-factor multiplication: The multiplication introduces a frequency slope, but the phase center position is not changed. Plot 3 represents the first convolution operation. This convolution tends to change the position of phase center and slope rate of the slope phase. The new phase center is the desired position denoted by the dotted line.

Subsequently, plot 4 illustrates the second phase-multiplication operation, which removes the modified frequency slopes. At this stage, the scaled phase term $(Cs + 1)rf_r$ is corrected to rf_r . The last convolution removes the residual phase that is generated by the aforementioned three operations shown in plots 2, 3, and 4 [13].

In Fig. 3, two chirp-signal multiplications and two chirp-signal convolutions provide the scale transform that is described in [16]–[18] in more detail. Based on the assumption of the positive chirp rate of the transmitted signal, the four parameters k_1, k_2, k_3 , and k_4 are given as

$$\begin{cases} k_1 = -c^2/(4K_s) \\ k_2 = c^2/(4CsK_s) \\ k_3 = c^2/[4(Cs + 1)K_s] \\ k_4 = -c^2/[4Cs(Cs + 1)K_s] \end{cases} \quad (27)$$

where K_s is defined by $1/K_s = 1/K_r + 1/K_{src}$. Replacing the frequency-scaling module in the block diagram of Fig. 2 with Fig. 3, according to [18], we can reduce the block diagram of Fig. 2 to the simplified one shown in Fig. 4.

Fig. 4 is the block diagram of the chirp scaling for the bistatic focusing in the constant-offset configuration. Where Ψ_1 , Ψ_2 , and Ψ_3 can be given as

$$\Psi_1(f_a, t) = \pi Cs K_s (t + t_m - t_{mc})^2 \quad (28)$$

$$\Psi_2(f_a, f) = \frac{\pi f^2}{(Cs + 1)K_s} + 2\pi(t_{mc} - t_m)f \quad (29)$$

$$\Psi_3(f_a, t, r) = \Phi_{aIV}(f_a) + 2\pi\Phi_{aV}(f_a)r - Cs(Cs + 1)K_s\pi t^2. \quad (30)$$

In (28) and (30), t represents the range time variable, given by $2r/c$. The multiplication of the first phasor equalizes the range curvature of all the points; the task of the second phasor is to focus the range signal and remove the equalized range curvature; the last one is used to focus the azimuth signal and compensate the residual phase.

The aforementioned three phase terms correspond well to the three phase terms presented in [13]. Thus, the monostatic CSA processor can be used to focus the bistatic data only with the adjustment of Doppler parameters.

In Section V, we will validate the CSA for the bistatic processing using simulated and real radar data.

IV. MOCO OF AIRBORNE BISATIC SAR IN THE CONSTANT-OFFSET CONFIGURATION

In this section, we investigate the model of the bistatic deviations and compensation method of the deviations. The actual instantaneous slant ranges from the antenna phase centers of receiver and transmitter to the point target $P(s_{0R}, R_{0R})$ can be expressed according to Fig. 5

$$\begin{aligned} \bar{R}_R(s) &= \sqrt{[R_{0R} + \delta r_{0R}(s, s_{0R})]^2 + v_R^2(s - s_{0R})^2} \\ &= R_R(s) + \delta R_R(s, s_{0R}, R_{0R}) \\ \bar{R}_T(s) &= \sqrt{[R_{0T} + \delta r_{0T}(s, s_{0T})]^2 + v_T^2(s - s_{0T})^2} \\ &= R_T(s) + \delta R_T(s, s_{0T}, R_{0T}) \end{aligned} \quad (31)$$

where δR_R and δR_T denote the instantaneous receiver-to-target and transmitter-to-target range displacements and δr_{0R} and δr_{0T} are the projections of δR_R and δR_T in ZDP that is perpendicular to nominal platform velocity vectors.

If δr_{0R} and δr_{0T} satisfy

$$\delta r_{0R} \ll \frac{\lambda}{8 \tan(\theta_{RS}/2)^2} \quad \delta r_{0T} \ll \frac{\lambda}{8 \tan(\theta_{TS}/2)^2}. \quad (32)$$

Using the Taylor approximation, (31) can be simplified as

$$\begin{aligned} \delta R_R(s, s_{0R}, R_{0R}) &= \left. \frac{\partial(\bar{R}_R - R_R)}{\partial(\delta r_{0R})} \right|_{\delta r_{0R}=0} \delta r_{0R}(s, R_{0R}) \approx \delta r_{0R}(s, R_{0R}) \\ \delta R_T(s, s_{0T}, R_{0T}) &= \left. \frac{\partial(\bar{R}_T - R_T)}{\partial(\delta r_{0T})} \right|_{\delta r_{0T}=0} \delta r_{0T}(s, R_{0T}) \approx \delta r_{0T}(s, R_{0T}). \end{aligned} \quad (33)$$

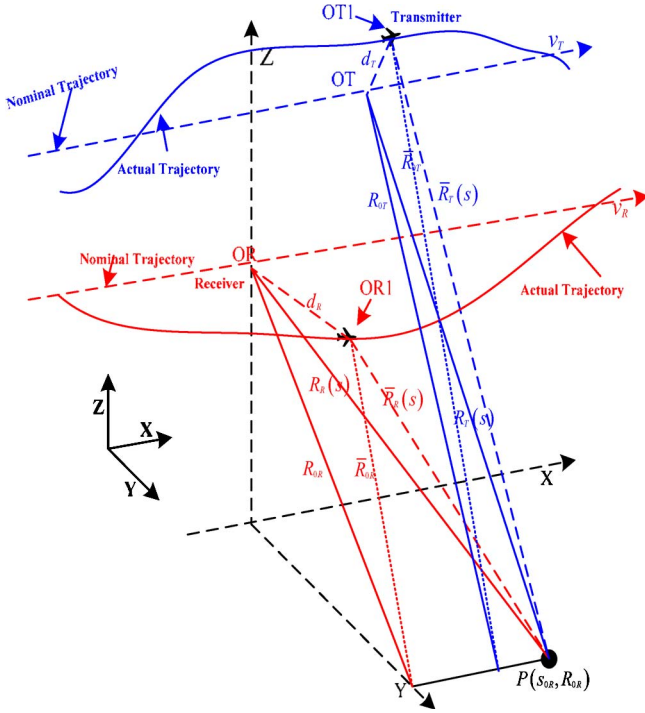


Fig. 5. Bistatic SAR geometry in the presence of trajectory deviations. The parameters corresponding to receiver and transmitter are denoted with the subscripts “R” and “T,” respectively. X , Y , and Z represent the along-track, cross-track, and vertical directions, respectively.

Equation (33) implies that the instantaneous range displacements for the target located in the bistatic composite footprint can be approximately projected into the ZDP, if the condition of the narrow beam is satisfied in the azimuth direction. Using the approximation, the dependence of the trajectory deviations on the azimuth coordinate of the target is disregarded.

To compensate the displacements, our main task is first to evaluate the displacements according to the actual 3-D geometry of bistatic SAR, as shown in Fig. 5. The deviation in the X -direction (i.e., the flight direction) accounts for along-track nominal velocity changes, which are generally compensated by azimuth resampling of the SAR raw data [14]. Therefore, we disregard the deviation in the X -direction in this paper. The deviations in the Y - and Z -directions might lead to the fact that the receiver and the transmitter deviate from the ideal positions “OR” and “OT” to the real position “OR1” and “OT1” in the ZDP, respectively (see in Fig. 5). The amounts of position deviation are denoted with d_R and d_T for receiver and transmitter, respectively. For clarity, the 2-D geometries of the position deviations in the ZDP are highlighted as shown in Fig. 6.

In Fig. 6, $d_R(s, R_{0R})$ and $d_T(s, R_{0T})$ are given as

$$\begin{aligned} d_R(s, R_{0R}) &= \Delta z_R \sin \vartheta_{Re} + \Delta y_R \cos \vartheta_{Re} \\ d_T(s, R_{0T}) &= \Delta z_T \sin \vartheta_{Te} + \Delta y_T \cos \vartheta_{Te} \end{aligned} \quad (34)$$

where Δz_R , Δy_R , Δz_T , and Δy_T represent the deviations of the receiver and transmitter in the Z and Y -direction, respectively; ϑ_{Re} and ϑ_{Te} are the angles relative to the Y -direction deviations. The aforementioned four deviations can be mea-

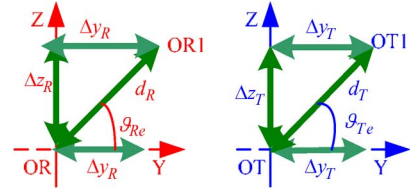


Fig. 6. Sensors' position deviations in ZDP. (Left) Receiver. (Right) Transmitter.

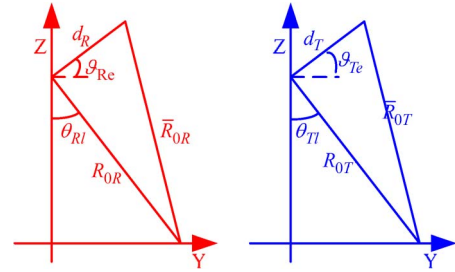


Fig. 7. Slant-range displacements caused by the trajectory deviations in ZDP. (Left) Receiver. (Right) Transmitter. θ_{Rl} and θ_{Tl} represent the depression angles of receiver and transmitter, respectively.

sured using the onboard INS and GPS. Therefore, $d_R(s, R_{0R})$ and $d_T(s, R_{0T})$ are available using the measured information. Based on $d_R(s, R_{0R})$ and $d_T(s, R_{0T})$, we can evaluate δr_{0R} and δr_{0T} using the 2-D geometries of range displacement, as shown in Fig. 7.

Using Fig. 7, the slant-range displacements in the ZDP can be expressed as

$$\begin{aligned} \delta r_{0R}(s, R_{0R}) &= \bar{R}_{0R} - R_{0R} \\ &= \sqrt{R_{0R}^2 + d_R^2 - 2d_R R_{0R} \sin(\theta_{Rl} - \vartheta_{Re})} - R_{0R} \\ \delta r_{0T}(s, R_{0T}) &= \bar{R}_{0T} - R_{0T} \\ &= \sqrt{R_{0T}^2 + d_T^2 - 2d_T R_{0T} \sin(\theta_{Tl} - \vartheta_{Te})} - R_{0T} \quad (35) \\ \delta r_B(s, R_m, r) &= \delta r_{0R}(s, R_{0R}) + \delta r_{0T}(s, R_{0T}) \\ &= \delta r_{0R}(s, r + R_m) + \delta r_{0T}[s, (c_0 - 1)R_m + (c_1 - 1)r]. \end{aligned} \quad (36)$$

The bistatic-displacement error generally introduces two influences: One is to generate an additional azimuth-modulation term, denoted by $\exp[-j2\pi\delta r_B/\lambda]$, another causes an erroneous RCMC, denoted by δr_B .¹ Therefore, MOCO must consist of two kinds of compensation: azimuth modulation and RCM. Both of two compensations are range-dependent.

¹ When δr_B is less than half of a range resolution cell, it is usually negligible.

When the error of RCM caused by δr_B is negligible, only the compensation of the range-dependent azimuth modulation is required, and it can easily be performed with the phase multiplication operation in the azimuth time domain and slant-range space domain after RCMC.

However, the case where RCM error is not negligible becomes more complex. To address this problem, in this paper, the monostatic SAR MOCO method is introduced [14], [15]. The basic idea is to decompose the bistatic range displacements δr_B into the range-invariant and range-variant components, namely

$$\delta r_B(s, R_m, r) = \delta r_{B_IV}(s) + \delta r_{B_V}(s, r) \quad (37)$$

where $\delta r_{B_IV}(s)$ denotes the range-invariant component and $\delta r_{B_V}(s, r)$ represents range-variant one. Because $\delta r_{B_IV}(s)$ is range-independent, it can be compensated flexibly before or after range compression. The range-invariant azimuth modulation can be removed by multiplying the azimuth signal in the azimuth time domain with the phase function

$$H_{MOCO Ia}(s) = \exp \left[j \frac{2\pi}{\lambda} \delta r_{B_IV}(s) \right]. \quad (38)$$

To optimize the efficiency of the processing procedure, the range-invariant RCM error can be corrected together with range compression in the range-frequency domain using a phase ramp function

$$H_{MOCO Ia}(s, f) = \exp \left[j \frac{2\pi}{c} f \delta r_{B_IV}(s) \right]. \quad (39)$$

After correcting the range-invariant RCM error, the residual range-variant component of RCM is assumed to have a limited impact on the RCMC.² Based on this assumption, only the range-variant azimuth-modulation error needs to be compensated after RCMC in the azimuth time domain by a phase function.

$$H_{MOCO II}(s, r) = \exp \left[j \frac{2\pi}{\lambda} \delta r_{B_V}(s, r) \right]. \quad (40)$$

Based on the earlier descriptions of the bistatic MOCO, the following two key points are summarized.

- 1) The range-invariant RCM error must be compensated before the compensation of the range-variant azimuth-modulation term.
- 2) The RCM error caused by the range-variant bistatic slant-range displacement must be kept within half of a range resolution cell.

After analyzing the model and processing procedure of bistatic SAR MOCO, we further integrate the presented method into the processing procedure of CSA. CSA is a chirp-based processing method, which requires that an azimuth Fourier transformation is performed first. Thus, the compensation of range-invariant RCM error is difficult to be combined with the range compression step, since the azimuth-modulation error is

²When the RCM error that is introduced by δr_{B_V} is greater than half of a range resolution cell, we can segment the range swath into blocks and keep the δr_{B_V} within half of a range resolution cell in every block.

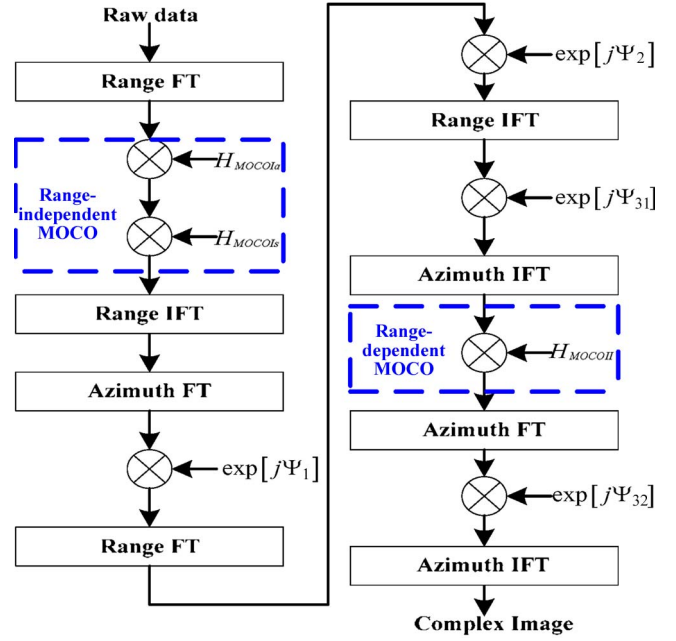


Fig. 8. Block diagram of CSA with MOCO.

dependent on the azimuth time variable and has to be compensated in the azimuth domain. In this paper, we additionally invest a pair of range FTs to compensate the range-invariant displacement before the azimuth FT.

Inspecting (30), we identify three phase terms in Ψ_3 : The first two terms account for the azimuth compression, the third one is a residual phase term. In order to compensate the range-variant azimuth-modulation term before the azimuth compression, we divide Ψ_3 into two parts

$$\Psi_3(f_a, t, r) = \Psi_{31}(f_a, t) + \Psi_{32}(f_a, r) \quad (41)$$

where

$$\begin{aligned} \Psi_{31}(f_a, t) &= -Cs(Cs + 1)K_s\pi t^2 \\ \Psi_{32}(f_a, r) &= \Phi_{aIV}(f_a) + 2\pi\Phi_{aV}(f_a)r. \end{aligned} \quad (42)$$

Then, a pair of additional azimuth FTs needs to be employed to compensate $H_{MOCO II}$ in the azimuth time domain, after removal of Ψ_{31} and before compensating the azimuth-modulation term Ψ_{32} . The block diagram of CSA with MOCO is shown in Fig. 8.

V. RESULTS OF POINT-TARGET SIMULATION AND REAL RADAR DATA PROCESSING

In this section, spaceborne and airborne simulations are carried out to validate the performance of CSA in the constant-offset configuration. In order to highlight the capacity of processing and the range-variant feature, the designed scene consists of five point targets orthogonal to the flight direction. Here, a flat Earth model is assumed, and geometry is shown in Fig. 9. The system parameters are listed in Table I.

To quantify the precision of processing, the impulse-response width (IRW), peak sidelobe ratio (PSLR), and integrated

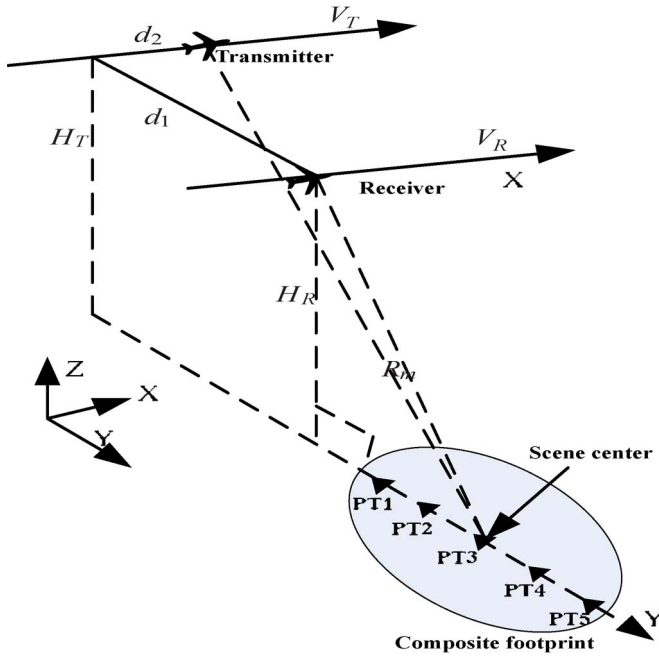


Fig. 9. Bistatic geometry with five point targets. PT3 is located in the scene center. X -, Y -, and Z -directions represent the along-track, horizontal, and vertical direction, respectively.

TABLE I
SPACEBORNE/AIRBORNE SYSTEM PARAMETERS

	Transmitter	Receiver
	Spaceborne/Airborne	
Carrier frequency	9.65/10.13 GHz	
Bandwidth	35/100 MHz	
PRF	3500/650 Hz	
Velocity	7000/110 m/s	
Azimuth beam width	0.33/1.6956 °	0.33/1.6956 °
Altitude	515/7.5 Km	515/7 Km
Depression angle	45.11/55 °	45/55.38 °
Cross-track offset(d_1)	2 Km/700 m	
Along-track offset(d_2)	2 Km/500 m	

TABLE II
QUALITY PARAMETERS OF IMPULSE-RESPONSE FUNCTION

	Range			Azimuth		
	IRW (m)	PSLR (dB)	ISLR (dB)	IRW (m)	PSLR (dB)	ISLR (dB)
PT1	4.3131	-13.21	-9.89	2.7096	-13.25	-9.68
PT2	4.3131	-13.12	-9.85	2.7096	-13.24	-9.67
PT3	4.3131	-13.14	-9.86	2.7096	-13.25	-9.67
PT4	4.3131	-13.17	-9.87	2.7096	-13.24	-9.67
PT5	4.3131	-13.19	-9.88	2.7096	-13.24	-9.69

sidelobe ratio (ISLR) are used as criteria. It needs to be emphasized that no weighting function is used in both directions.

A. Spaceborne Simulation

In the spaceborne simulation, the simulated point targets have the relative receiver-to-target slant ranges: -6.4 , -2.8 , 0 , 2.8 , and 6.4 km with respect to that of PT3. The theoretical IRW in range and azimuth are 4.2827 and 2.6969 m, respectively. Table II lists the measured quality parameters of the focused scene.

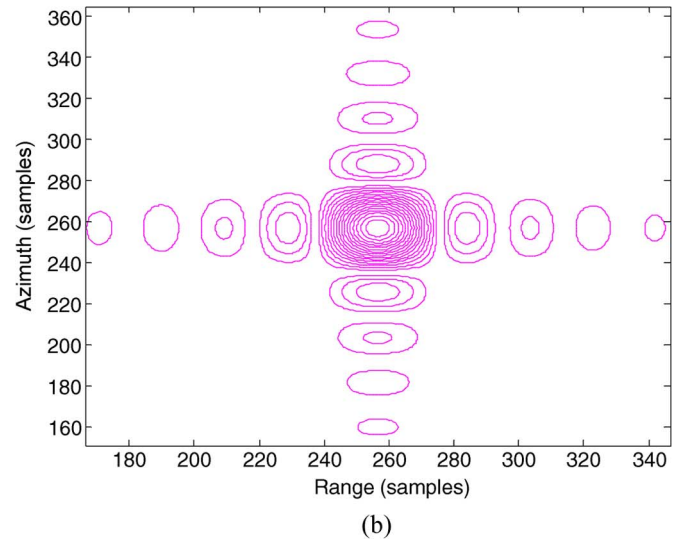
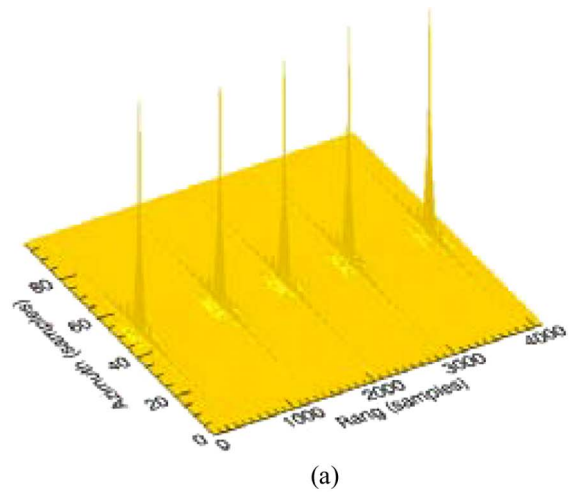


Fig. 10. (a) Focusing results for the spaceborne TI_{GC} configuration. (b) Close look at the rightmost point target (PT5).

Examining Table II, it can be seen that the deviations of the PSLRs and ISLRs in both directions are within 0.1 dB of the theoretical values of -13.2 and -9.7 dB, respectively. The measured azimuth and range resolutions have a maximum broadening of about 0.47% and 0.71% , respectively. Furthermore, Fig. 10(a) shows the corresponding focusing results of the whole scene. The targets located in the leftmost and rightmost are PT1 and PT5, respectively. Furthermore, the rightmost point target PT5 is examined in more detail in Fig. 10(b).

Based on the preceding results, it can be seen that the processing results with the proposed method agree well with the theoretical value in the constant-offset spaceborne configuration.

B. Airborne Simulation and Real Airborne SAR Data Processing

1) *Simulation Experiment:* In airborne experiment, the simulated point targets have the relative receiver-to-target slant ranges: -2.0 , -0.9 , 0 , 0.9 , and 2.0 km with respect to that of PT3. The experiment without the trajectory deviation is performed first. For this simulation, the theoretical IRW in the

TABLE III
QUALITY PARAMETERS OF IMPULSE-RESPONSE FUNCTION
IN THE AIRBORNE CONFIGURATION

	Range			Azimuth		
	IRW (m)	PSLR (dB)	ISLR (dB)	IRW (m)	PSLR (dB)	ISLR (dB)
PT1	1.5025	-13.26	-9.86	0.5148	-13.24	-9.71
PT2	1.5025	-13.25	-9.83	0.5148	-13.25	-9.74
PT3	1.5025	-13.27	-9.87	0.5148	-13.27	-9.75
PT4	1.5025	-13.27	-9.87	0.5148	-13.26	-9.75
PT5	1.5025	-13.24	-9.85	0.5148	-13.24	-9.74

TABLE IV
QUALITY PARAMETERS USING CSA WITHOUT MOCO

	Range			Azimuth		
	IRW (m)	PSLR (dB)	ISLR (dB)	IRW (m)	PSLR(dB)	ISLR (dB)
PT1	1.5025	-13.34	-9.77	0.5148	-13.04	-9.62
PT2	1.5025	-13.18	-9.27	0.5365	-9.03	-6.48
PT3	1.5025	-13.04	-9.70	1.1892	-3.56	-1.16
PT4	1.5025	-13.14	-9.41	2.6829	-1.93	-0.49
PT5	1.5025	-13.03	-9.60	4.2927	-2.62	-3.02

TABLE V
QUALITY PARAMETERS USING CSA WITH THE
RANGE-INDEPENDENT MOCO

	Range			Azimuth		
	IRW (m)	PSLR (dB)	ISLR (dB)	IRW (m)	PSLR (dB)	ISLR (dB)
PT1	1.5025	-13.17	-9.59	0.6163	-6.18	-3.84
PT2	1.5025	-13.18	-9.56	0.5220	-10.70	-7.91
PT3	1.5025	-13.27	-9.84	0.5148	-13.24	-9.74
PT4	1.5025	-13.19	-9.48	0.5293	-10.18	7.55
PT5	1.5025	-13.22	-9.78	0.9136	-4.15	-1.80

TABLE VI
QUALITY PARAMETERS USING CSA WITH THE TOTAL MOCO

	Range			Azimuth		
	IRW (m)	PSLR (dB)	ISLR (dB)	IRW (m)	PSLR (dB)	ISLR (dB)
PT1	1.5025	-13.23	-9.86	0.5148	-13.22	-9.70
PT2	1.5025	-13.25	-9.85	0.5148	-13.26	-9.74
PT3	1.5025	-13.27	-9.87	0.5148	-13.24	-9.74
PT4	1.5025	-13.26	-9.87	0.5148	-13.25	-9.76
PT5	1.5025	-13.25	-9.88	0.5148	-13.24	-9.66

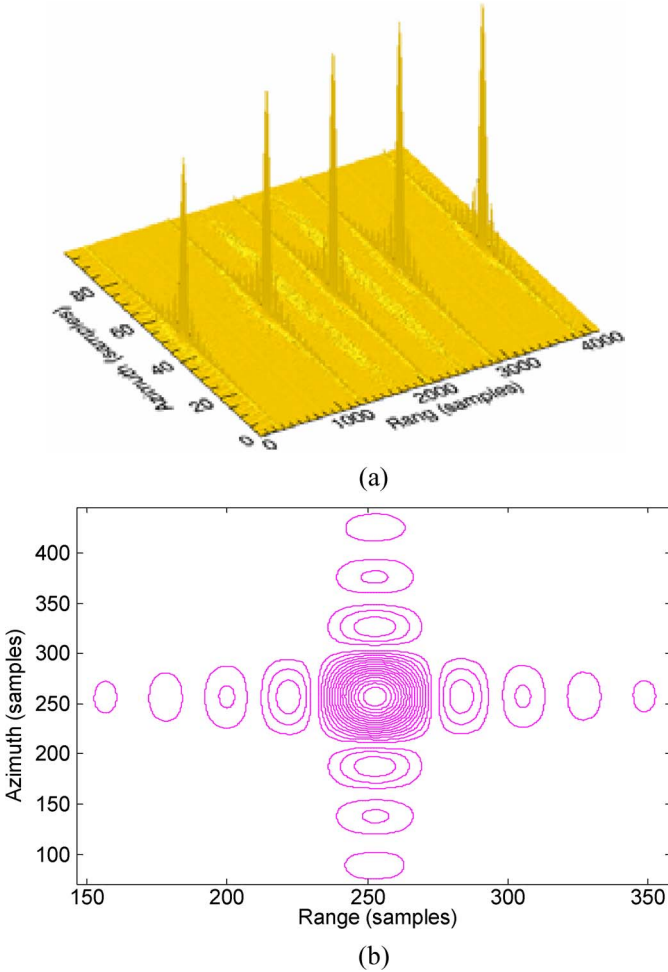


Fig. 11. (a) Focusing results for the airborne TI_GC configuration. (b) Close look at the rightmost point target (PT5).

range and azimuth directions are 1.5 and 0.5137 m, respectively. The measured parameters are listed in Table III.

Examining Table III, we see that the ISLRs in range direction deviate within 0.1 dB of the theoretical value of -9.7 dB. The measured azimuth and range resolutions have a maximum broadening of about 0.21% and 0.17%, respectively. Furthermore, Fig. 11(a) shows the corresponding focusing results of the scene. The targets located in the leftmost and rightmost are still PT1 and PT5, respectively. Point target PT5 is analyzed in more detail in Fig. 11(b).

To validate the MOCO method developed in this paper, some simulations about the trajectory deviations are carried out.

In this simulation, we introduce the sinusoidal deviations in Z (vertical track)- and Y (cross track)-directions (cf. Fig. 5). For the receiver, we assume a pure Z -direction deviation, while for the transmitter, we assume a pure Y -direction. Both sinusoidal deviations exhibit 0.13 cycle per synthetic-aperture time. The amplitudes are 3 m for the Z -direction and 2.8 m for the Y -direction.

In this simulation, we choose the bistatic displacement of point target PT3 as the invariant component δr_{B_IV} . Using the trajectory deviations, the measured parameters in the following three cases are listed in Tables IV–VI: 1) without MOCO, cf. Table IV, 2) range-independent MOCO, cf. Table V, and 3) range-independent and range-dependent MOCO, cf. Table VI.

Table IV shows that the azimuth impulse response suffers from significant degradation, and the range impulse response is slightly degraded. The azimuth quality of focused targets degrades sensibly from near range to far range along the swath. The variant degradation can be explained by using Fig. 12(c) where the absolute amounts of the bistatic slant-range displacement becomes more and more serious from near range to far range.

Table V demonstrates the results after compensating the range-invariant displacements. Examining the quality parameters listed in Table V, it can be seen that the azimuth impulse

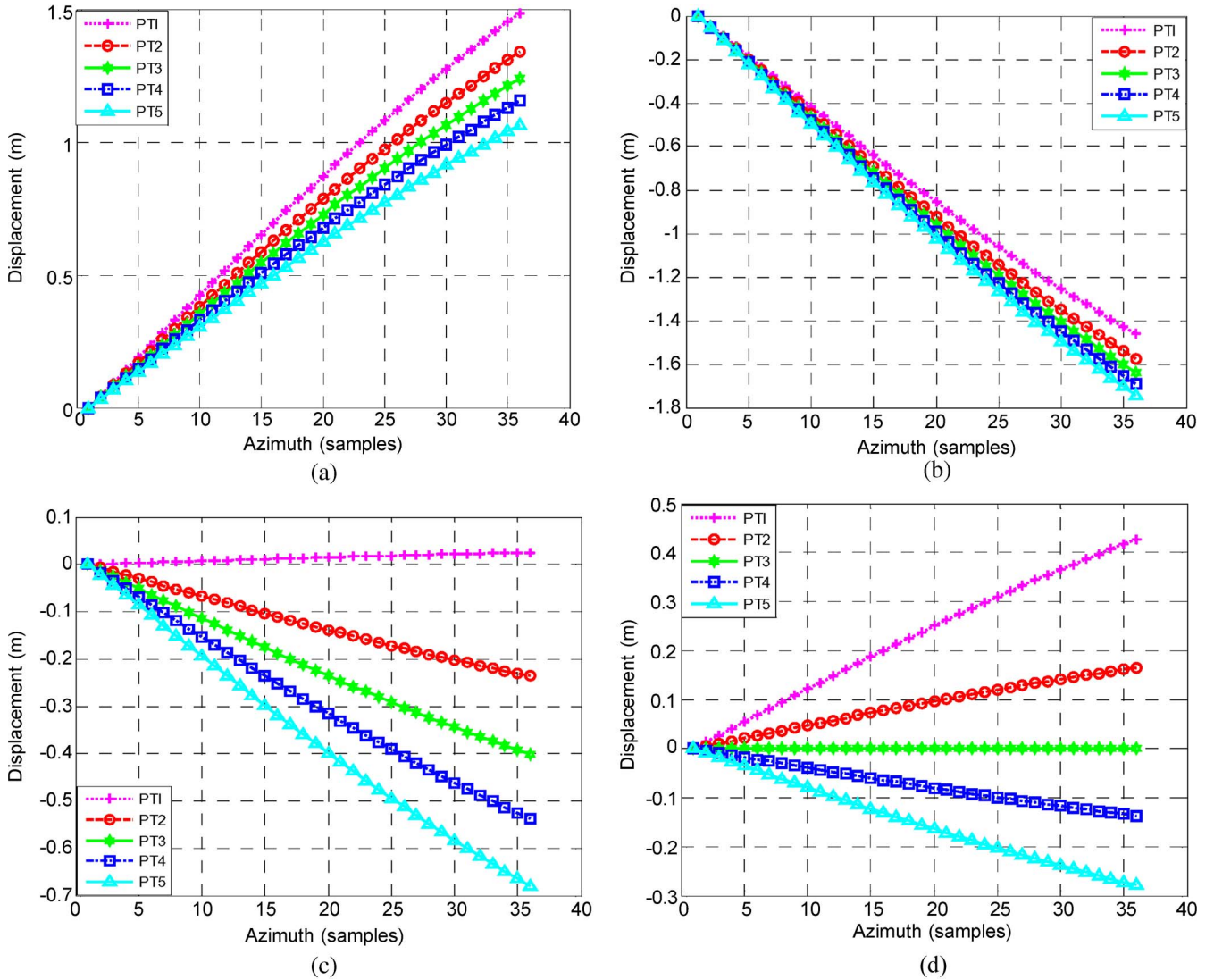


Fig. 12. (a) Receiver-to-target range displacement. (b) Transmitter-to-target range displacements. (c) Bistatic range displacements of PT1–PT5. (d) Range-variant bistatic range displacements of PT1–PT5.

response of PT1 spreads more seriously with respect to the case without the range-invariant MOCO. The reason for this spreading is that if the range-invariant displacement is two times greater than the displacement of its bistatic range displacement, a bigger displacement error can be introduced after the range-invariant component is removed [see (37)]. This interpretation can be verified by comparing Fig. 12(c) and (d) (Fig. 12(a) and (b) shows the individual range displacements of receiver and transmitter, respectively). In Fig. 12(c), the displacement of PT3 is more than two times greater than that of PT1. Thus, the range-variant component of PT1, shown in Fig. 12(d), is greater than its original displacement, shown in Fig. 12(c). The targets located in far range show an improvement in terms of azimuth resolution, PSLR and ISLR with respect to the non-MOCO case since their range-variant components δr_{B_V} are a little less than their original displacements δr_B .

For the compensation of the range-variant displacement, we neglect its effect on the RCM. This is justified only if the range-variant component is less than half of a range resolution cell. In this simulation, the half of the theoretical resolution cell

is equal to 0.75 m which is larger than the maximum of the range-variant displacements of 0.4308 m. Therefore, using the processing procedure shown in Fig. 8 yields a good focusing result after compensating the final range-variant component, as demonstrated by Table VI.

2) *Real Bistatic Airborne SAR Data Processing*: This section presents the processing results of real bistatic SAR data. The data have been acquired by the German Research Establishment for Applied Natural Sciences (FGAN) Phased Array Multifunctional Imaging Radar and Airborne Experimental Radar in November 2003. Both transmitter and receiver work at X-band and share a common bandwidth of 300 MHz. The bistatic flight experiment has a bistatic angle of 13° [3], [5]. However, because of the complex flight condition, the along-track offset is slightly time varying and not constant; we only treat the offset as nearly constant over a short azimuth time [3].

Fig. 13 shows the processing results without MOCO and with MOCO. The left figure blurs slightly with respect to the right one. From Fig. 13, it is shown that using MOCO yields a shaper image.

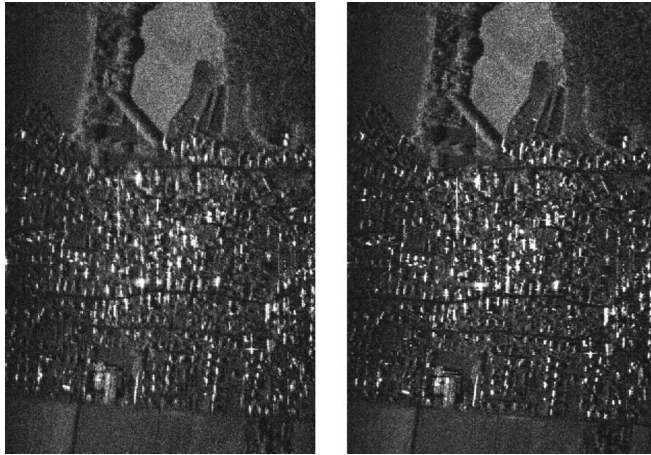


Fig. 13. CSA processing using raw data FGAN-FHR. (Left) Without MOCO. (Right) With the proposed MOCO. The horizontal and vertical directions denote the range and azimuth, respectively.

VI. CONCLUSION

This paper presented a chirp-scaling approach to the processing of bistatic SAR data for constant-offset configurations. The inherent difference in the point-target reference spectrum between monostatic and bistatic SARs makes monostatic SAR processing algorithms not directly applied to handle bistatic SAR data. The basic is to decompose the QM and the BD terms into range-variant and range-invariant components and, then, to incorporate BD term into the QM term. The decomposition and incorporation manipulations make any monostatic processing algorithm applicable only with an adjustment of the Doppler parameters. Thus, the proposed method meets the requirements of precision and efficiency.

For airborne bistatic SAR systems, MOCO is necessary. In this paper, the position deviations of two platforms are modeled as the bistatic slant-range displacements in the ZDP, and then, the conventional two-step monostatic MOCO method is introduced to correct the bistatic range displacement. Simulations show that the presented method and model are effective.

ACKNOWLEDGMENT

This work reported herein is part of the joint DFG (German Science Foundation) research initiative Bistatic Exploration (PAK 59) of ZESS and FGAN. The authors would furthermore like to point out the excellent and very effective cooperation between ZESS and FHR/FGAN, which is seen as a key item of their work. The authors would like to thank the anonymous reviewers for their very constructive and encouraging criticism, helping to improve the final paper.

REFERENCES

- [1] O. Loffeld, H. Nies, V. Peters, and S. Knedlik, "Models and useful relations for bistatic SAR processing," *IEEE Trans. Geosci. Remote Sens.*, vol. 42, no. 10, pp. 2031–2038, Oct. 2004.
- [2] K. Natroshvili, O. Loffeld, H. Nies, A. M. Ortiz, and S. Knedlik, "Focusing of general bistatic SAR configuration data with 2-D inverse scaled FFT," *IEEE Trans. Geosci. Remote Sens.*, vol. 44, no. 10, pp. 2718–2727, Oct. 2006.

- [3] H. Nies, O. Loffeld, and K. Natroshvili, "Analysis and focusing of bistatic airborne SAR data," *IEEE Trans. Geosci. Remote Sens.*, vol. 45, no. 11, pp. 3342–3349, Nov. 2007.
- [4] D. D'Aria, A. M. Guarnieri, and F. Rocca, "Focusing bistatic synthetic aperture radar using Dip Move Out," *IEEE Trans. Geosci. Remote Sens.*, vol. 42, no. 7, pp. 1362–1376, Jul. 2004.
- [5] I. Walterscheid, J. H. G. Ender, A. R. Brenner, and O. Loffeld, "Bistatic SAR processing and experiments," *IEEE Trans. Geosci. Remote Sens.*, vol. 44, no. 10, pp. 2710–2717, Oct. 2006.
- [6] V. Giroux, H. Cantalloube, and F. Daout, "An omega-K algorithm for SAR bistatic systems," in *Proc. IGARSS*, Seoul, Korea, Jul. 2005, pp. 1060–1063.
- [7] M. Rodríguez-Cassolá, G. Krieger, and M. Wendler, "Azimuth-invariant, bistatic airborne SAR processing strategies based on monostatic algorithms," in *Proc. IGARSS*, Seoul, Korea, Jul. 2005, pp. 1047–1050.
- [8] R. Bamler, F. Meyer, and W. Liebhart, "Processing of bistatic SAR data from quasi-stationary configurations," *IEEE Trans. Geosci. Remote Sens.*, vol. 45, no. 11, pp. 3350–3358, Nov. 2007.
- [9] M. Antoniou, R. Saini, and M. Cherniakov, "Results of a space-surface bistatic SAR image formation algorithm," *IEEE Trans. Geosci. Remote Sens.*, vol. 45, no. 11, pp. 3359–3371, Nov. 2007.
- [10] Y. L. Neo, F. Wong, and I. G. Cumming, "A two-dimensional spectrum for bistatic SAR processing using series reversion," *IEEE Geosci. Remote Sens. Lett.*, vol. 4, no. 1, pp. 93–96, Jan. 2007.
- [11] Y. L. Neo, "Geometries and processing algorithms for bistatic SAR," Ph.D. dissertation, Dept. Elect. Comput. Eng., British Columbia Univ., Vancouver, BC Canada, 2006.
- [12] I. G. Cumming and F. H. Wong, *Digital Processing of Synthetic Aperture Radar Data Algorithms and Implementation*. Norwood, MA: Artech House, 2005.
- [13] R. K. Raney, H. Runge, R. Bamler, I. G. Cumming, and F. H. Wong, "Precision SAR processing using chirp scaling," *IEEE Trans. Geosci. Remote Sens.*, vol. 32, no. 4, pp. 786–799, Jul. 1994.
- [14] G. Fornaro, G. Franceschetti, and S. Perna, "Trajectory deviations in airborne SAR: Analysis and compensation," *IEEE Trans. Aerosp. Electron. Syst.*, vol. 35, no. 7, pp. 997–1009, Jul. 1999.
- [15] A. Moreira and Y. H. Huang, "Airborne SAR processing of highly squinted data using a chirp scaling approach with integrated motion compensation," *IEEE Trans. Geosci. Remote Sens.*, vol. 32, no. 10, pp. 1029–1040, Sep. 1994.
- [16] G. Franceschetti and R. Lanari, *Synthetic Aperture Radar Processing*. Boca Raton, FL: CRC Press, 1999.
- [17] A. Papoulis, *Systems and Transforms with Applications in Optics*. New York: McGraw-Hill, 1968.
- [18] R. Lanari and G. Fornaro, "A short discussion on the exact compensation of the SAR range-dependent range cell migration effect," *IEEE Trans. Geosci. Remote Sens.*, vol. 35, no. 6, pp. 1446–1452, Nov. 1997.



Robert Wang (M'07) received the B.S. degree in control engineering from the University of Henan, Kaifeng, China, in 2002 and the Dr. Eng. degree from the Graduate University of Chinese Academy of Sciences, Beijing, China, in 2007.

Since 2007, he has been with the Center for Sensorsystems (ZESS), University of Siegen, Siegen, Germany, where he is currently working at the hybrid bistatic experiment. His current research interests include monostatic and bistatic SAR signal processing, bistatic interferometric airborne SAR motion compensation, and SAR raw-signal simulation.



Otmar Loffeld (M'05–SM'06) received the Diploma degree in electrical engineering from the Technical University of Aachen, Aachen, Germany, in 1982 and the Eng.Dr. and the “Habilitation” degrees in the field of digital signal processing and estimation theory from the University of Siegen, Siegen, Germany, in 1986 and 1989, respectively.

Since 1991, he has been a Professor of digital signal processing and estimation theory with the University of Siegen, where he has been giving lectures on general communication theory, digital signal

processing, stochastic models and estimation theory, and synthetic aperture radar. In 1995, he became a member of the Center for Sensorsystems (ZESS), which is a central scientific research establishment at the University of Siegen (www.zess.uni-siegen.de), where since 2005, he has been the Chairman. He is author of two textbooks on estimation theory. In 1999, he was a Principal Investigator (PI) on Baseline Estimation for the X-band part of the Shuttle Radar Topography Mission where ZESS contributed to DLR's baseline-calibration algorithms. He is PI for interferometric techniques in the German TerraSAR-X mission, and, together with Prof. Ender from Forschungsgesellschaft für Angewandte Naturwissenschaften (FGAN), he is one of the PIs for a bistatic spaceborne-airborne experiment, where TerraSAR-X serves as the bistatic illuminator while FGAN's PAMIR system mounted on a Transall airplane is used as a bistatic receiver. In 2002, he founded the International Postgraduate Program “Multi Sensorics,” and based on that program, he established the “NRW Research School on Multi Modal Sensor Systems for Environmental Exploration and Safety (www.moses-research.de)” at the University of Siegen as an upgrade of excellence, in 2008. He is the Speaker and Coordinator of both doctoral degree programs, hosted by ZESS. Furthermore, he is the university's Scientific Coordinator for “Multidimensional and Imaging Systems.” His current research interests include multisensor data fusion, Kalman filtering techniques for data fusion, optimal filtering and process identification, SAR processing and simulation, SAR interferometry, phase unwrapping, and baseline estimation. A recent field of interest is bistatic SAR processing.

Prof. Loffeld is a member of the ITG/VDE and Senior Member of the IEEE/GRSS. He was the recipient of the Scientific Research Award of Northrhine–Westphalia (“Bennigsen–Foerder Preis”) for his works on applying Kalman filters to phase-estimation problems such as Doppler centroid estimation in SAR, phase, and frequency demodulation.



Holger Nies received the Diploma degree in electrical engineering and the Dr. Eng. degree from the University of Siegen, Siegen, Germany, in 1999 and 2006, respectively.

Since 1999, he has been a member of the Center for Sensorsystems (ZESS), University of Siegen, and a Lecturer with the Department of Signal Processing and Communication Theory. He worked in the project sector “Optimal Signal Processing, Remote Sensing—SAR” of ZESS in 1999. He was also involved in some project work for Daimler AG, Stuttgart, Germany, in the field of engine modeling and optimization. He is currently working in the area of interferometric techniques in the German TerraSAR-X mission. His current research interests include bistatic SAR processing, SAR interferometry, and distributed data fusion.

Dr. Nies was a recipient of the Best Poster Award at the Sixth European Conference on Synthetic Aperture Radar (EUSAR), Dresden, Germany, in 2006.



Stefan Knedlik (M'04) received the Diploma degree in electrical engineering and the Dr. Eng. degree from the University of Siegen, Siegen, Germany, in 1998 and 2003, respectively.

Since 1998, he has been a member of the Center for Sensorsystems (ZESS), University of Siegen, and a Researcher and Lecturer with the Department of Signal Processing and Communication Theory. Since 2002, he has also been the Executive Director of the International Postgraduate Programme IPP Multi Sensorics. Within the IPP Multi Sensorics,

he founded a research group on navigation. His current research interests include signal processing and applied estimation theory in navigation and SAR processing.



Joachim H. G. Ender (M'02–SM'06) received the Diploma degree in mathematics and physics from the Westphalian Wilhelm University, Münster, Germany, in 1975 and the Ph.D. degree in electrical engineering from Ruhr-University Bochum, Bochum, Germany.

In 1976, he was with the Forschungsgesellschaft für Angewandte Naturwissenschaften (FGAN), Wachtberg, Germany, which is also known as Research Establishment of Applied Science. Since 1992, he has been giving annual lectures on radar signal processing with Ruhr-University Bochum, which conferred the title Honorary Professor upon him in 2002. He also gives lectures on radar techniques with the Rhineish–Westphalian Technical-University, Aachen, Germany, and the University of Siegen, Siegen, Germany. In 1999, he was the Head with the Electronics Department, Research Institute for High Frequency Physics and Radar Techniques (FHR), FGAN, where he initiated and supervised research activities for various aspects of phased array and imaging radars, including the design and operation of experimental SAR systems, such as AER-II and PAMIR. Since 2003, he has been the Director of FHR, and he was elected Vice Chairman of FGAN in August 2007. His current research interests include very high resolution SAR imaging, 3-D SAR, MIMO SAR, multibaseline and wideband processing techniques for across-track SAR interferometry, ground moving-target indication with air- and space-based radar including multistatic satellite constellations, inverse SAR for moving-target imaging, and bistatic SAR processing. He authored and coauthored numerous papers in various international journals and conferences.

Dr. Ender is an executive board member of the German Institute of Navigation as well as Member-at-Large of North Atlantic Treaty Organization Sensors and Electronics Technology research panel. He further acts as Review Board Member of the German Research Foundation and as a Review Board Member of the Leibniz Society. He, jointly with colleagues, was the recipient of the German Society for Information Technology Paper Prize Award of the Association of German Electrical Engineers in 1992 and the IEEE TRANSACTIONS ON GEOSCIENCE AND REMOTE SENSING Best Paper Award in 2006. In 1996, he was one of the founding members of the biannual “European Conference on Synthetic Aperture Radar.”